Directional Analysis of SAR Images Aiming at Wind Direction

Wolfgang Koch

***Abstract*—Currently, the retrieval of wind fields from synthetic aperture radar (SAR) images suffers from inadequate knowledge of the wind direction. State-of-the-art spectral analysis works fine on open seas, but is limited in spatial resolution. The method described here is based on the local gradients computed with standard image processing algorithms. It handles image features not caused by wind and can be applied to irregularly shaped regions. The new method has already been applied to many images from the European Remote sensing Satellite SARs and RADARSAT-1 ScanSAR, usually supplying reasonable wind fields. The spatial sampling most frequently used was 20×20 and 10×10 km^2. In some cases, samplings down to 1×1 km^2 were tested. This paper describes the local gradients method including the filtering of nonwind generated image features and gives some application examples.**

***Index Terms*—Automatic wind direction retrieval, image filtering, image processing, numerical recipe, ocean winds, synthetic aperture radar (SAR), wind streaks.**

I. Introduction

ONE OF THE MAIN obstacles for the derivation of wind speeds from synthetic aperture radar (SAR) images is the lack of knowledge of the wind direction. Methods in use are, for example, assuming a fixed direction from a measurement for the whole image, or interpolation of the direction of wind fields from numerical weather models [1]–[3]. Neither method is really satisfying, as the information is too sparse and generally not at the right time. Estimating the wind direction directly from the SAR image is a much more attractive approach. This opportunity arises because there are several physical effects causing features in SAR images that are aligned with the wind direction, e.g., boundary layer rolls [4], [5], Langmuir cells, surfactant streaks, foam and water blown from breaking waves, or wind shadowing. The spacing of the boundary layer rolls in the cross-wind direction is reported to be from 1–9 km, depending on the properties of the marine boundary layer. Levy and Brown [6] state that boundary layer rolls were present in 44% and absent in 34% of 1882 SAR images. Wind shadows at lee coasts or behind marine platforms allow for the distinction of the up and down wind direction.

Spectral methods for estimation of wind directions in SEASAT SAR images were demonstrated in [4]. Application on ERS SAR images was shown in [7]–[9], and [10]. Standard deviations of the directional differences reported were between 10° and 37°. The spectral method works fine on open oceans, and large image areas, such as 20×20 km^2.

Working in the spatial domain by evaluating the local gradients, the new method automatically localizes features not caused by wind and ignores the affected points. The means for locating ocean features are given in this paper, while the land sea discrimination is done using coastline data, e.g., from the generic mapping tool [11].

As no specific shape of the evaluated subimages is required, it can be chosen to match the grid cells of a numerical atmospheric model. This simplifies the comparison with model winds or the assimilation into wind models by omitting the spatial interpolation. We compared modeled wind vectors with wind directions from the local gradients of 159 image products from the European Remote sensing Satellites 1 and 2 (ERS-1 and ERS-2). In total, the directional error was 17.6° with a bias of $-0.5°$, and a clear trend of the error to decrease with increasing wind speed was observed.

Last, but not least, the new method in particular cases allows a spatial sampling down to 1×1 km^2.

II. Local Gradients Method

The ideal image of a streak is about constant along its direction and strongest varying about orthogonal to its direction. As the direction of strongest increase is given by the gradient, the direction of a wind streak is about orthogonal to the gradient direction. The wind direction, assumed to be parallel to the wind streak, is thus also perpendicular to the direction of the gradient. Although due to the multiplicative noise present in SAR images, any gradient direction could be present, there is a preference toward the correct orthogonal direction. Thus the new method computes the local gradients with standard image processing algorithms, and chooses the orthogonal of the most frequent gradient direction to be a possible wind direction. In analogy to the spectral method, where the signal of the wind streaks was searched for at wavelengths from 500–1500 m, the gradients are computed on SAR images reduced to 100-, 200-, and 400-m pixels. Fig. 1 shows an example for a 5-km sampled wind field with directions computed from 100-m pixels. The scene was acquired by the ERS-1 SAR on August 12, 1991, 21 : 08. Wind streaks are visible all over the image. Wind shadows are apparent east of the island. Wind reported from a meteorological station at Cape Arkona at the north tip of Rügen was more than 10 m/s from 282°. At a couple of locations the nonambiguous directions were manually selected, while at the other subimages

Manuscript received March 28, 2002; revised February 17, 2003. This work was supported in part by the GKSS Research Center and in part by the German Bundesministerium für Bildung und Forschung (BMBF) under the project ENVOC.

The author is with the Department of Data Analysis and Data Assimilation (KSD), GKSS Research Center, D-21502 Geesthacht, Germany (e-mail: wolfgang.koch@gkss.de).

Digital Object Identifier 10.1109/TGRS.2003.818811

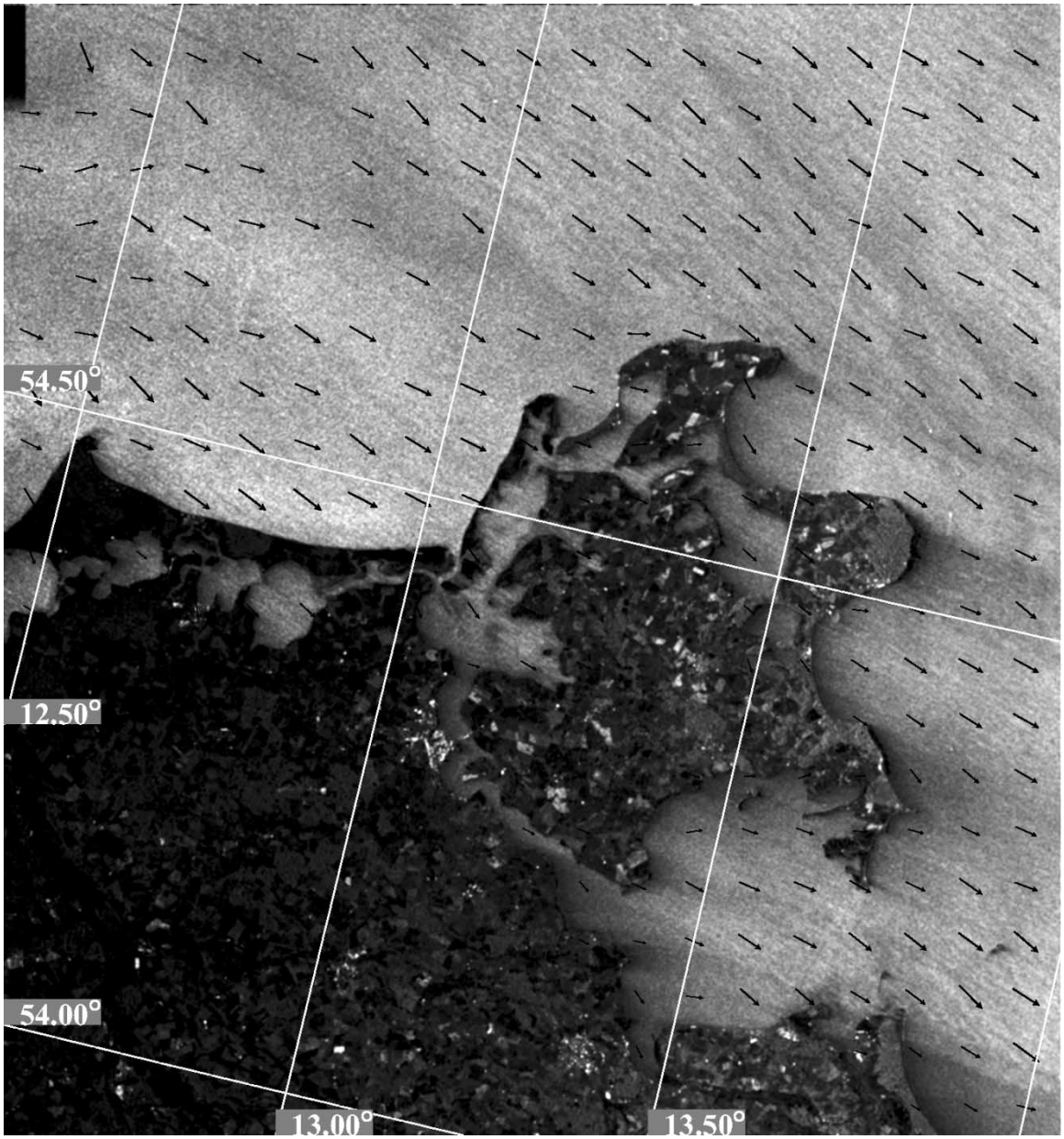

Fig. 1. ERS-1 SAR image of Rügen from August 12, 1991, 21 : 08. Wind streaks are visible over the entire image. Wind shadows are apparent east of the island. Wind reported from Cape Arkona at the northern tip of Rügen was more than 10 m/s from 282°. The black arrows are wind vectors computed from the image on a 5-km grid.

the directions were automatically selected to align with already unique directions at adjacent subimages. Some wind vectors were manually removed because they were obviously wrong, but the remaining wind vectors form a flow pattern that is consistent with the measured wind direction, and with the wind streaks and shadows visible in the image. This is a strong indication that the computed directions are indeed the wind directions.

A. Reducing the Image Size

The new directional analysis acts on SAR amplitude images reduced to 100-, 200-, and 400-m pixels. Image reductions to half size are done with the operator $R_{|2}$ throughout this paper. The operator $R_{|2}$ comprises smoothing of the image, resampling, and once again smoothing. Its exact definition is given in (33) in the Appendix. However, most of the SAR images do not come as amplitudes on 100-m pixels. Hence, they need some preparation before the analysis can start.

- RADARSAT ScanSAR images are provided as matrix of indices of a lookup table for the normalized radar cross section (NRCS), e.g., on 50×50 m^2 pixels. The square roots of the NRCS were taken as image amplitudes. The images were reduced to 100×100 m^2 pixels with $R_{|2}$.
- ERS SAR precision images (PRI) give amplitudes on 12.5×12.5 m^2 pixels. The image reduction was done by $R_{|2}^3$.
- ERS single-look complex (SLC) images give complex amplitudes. The pixels projected on the ground range are about 20×4 m^2. The roots of the averaged squared magnitudes of 1×5 pixels were used to come to 20×20 m^2

pixels. The image reduction to 100×100 m^2 pixels was done with

$$B^2 S_{|5} \left(B_{2y}^2 B_{2(x+y)}^2 B_{2(x-y)}^2 B_{2x}^2 \right)^2 \left(B_y^2 B_{x+y}^2 B_{x-y}^2 B_x^2 \right)^2 .$$

For the definitions of the operators, please refer to the Appendix.

The operations suggested above approximate isotropic lowpass filters, whereas for example box averaging does not. In the worst case box averaging may yield moire effects, e.g., see [12, ch. 10] or [13]. Although the noise present in SAR images will obscure moire effects, it is suggested to avoid box averaging.

B. Computing the Local Gradients

The components of the gradient are computed with the optimized Sobel operators

$$D_x = \frac{1}{32} \begin{pmatrix} 3 & 0 & -3 \\ 10 & 0 & -10 \\ 3 & 0 & -3 \end{pmatrix} \tag{1}$$

and its transpose.

$$D_y = D_x^T. \tag{2}$$

Using (1) and (2), the gradients are computed from the amplitude image A, stored as complex numbers (3) and squared. Hence, any gradient and its negative yield the same value. This operation will later be compensated by taking the square root, but meanwhile saves any special considerations for 180° ambiguities. As (1) and (2) imply already some smoothing, the image of squared gradients is reduced and smoothed with $R_{|2}$ (4). The same smoothing and reduction is done for the magnitudes of the squared gradients (5). From the triangular inequality, it is clear that the magnitude of the average (4) is smaller than the average of the magnitudes (5), and the better the squared gradients agree, the lesser is the difference. Where the gradient is nonzero, the quotient is thus taken as a measure of directional coherency (6)

$$G' = (g'_{mn}) = (D_x + iD_y)(A) \tag{3}$$

$$G'' = (g''_{m'n'}) = R_{|2} \left(\left(g'^2_{mn} \right) \right) \tag{4}$$

$$G''' = (g'''_{m'n'}) = R_{|2} \left(\left(\left| g'^2_{mn} \right| \right) \right) \tag{5}$$

$$0 \le c_{m'n'} = \frac{|g''_{m'n'}|}{g'''_{m'n'}} \le 1. \tag{6}$$

The systematic errors in the retrieved directions are shown for some operators in the textbook of Jähne [12, ch. 11]. The error is tested by applying the operators on a circular test pattern with wavenumbers smaller than 0.7 times the Nyquist wavenumber. With errors being between $-0.7°$ and $+0.7°$, the optimized Sobel operators (1) and (2) are much better than the common Sobel operators with errors between $-7°$ and $+7°$. Furthermore, the effect of noise on the directional error is relative small, so the optimized Sobel is accurate and robust as well. So, it is crucial not to replace the optimized Sobel operators with simple Sobel operators or differences, because that would dramatically increase the directional error.

C. Unusable Points

Having computed all local gradients, the values corresponding to the following points are discarded.

- The first and last two rows and columns of the image, because as mentioned in the Appendix, the convolutions applied are exact only at inner image points.
- *Land points:* The coastline database of the generic mapping tool [11] may be used for the land–sea discrimination.
- Points corresponding to nonwind features, if necessary, as localized for instance by the automatic algorithm given in Section III.

D. Extracting the Main Directions

The main direction for a subimage is determined by the position of the maximum in the smoothed histogram of weighted usable local gradients. For each defined subimage, this yields three values stemming from the different pixel sizes used. The scheme given below resulted after testing several different numbers of histogram intervals, different powers for the weights, and different smoothing. It works with only a few and with ten thousands of gradients.

For the usable points belonging to the selected subimage, a second quality measure is computed from the magnitudes of the directional information (4)

$$0 \le r_{m'n'} = \frac{|g''_{m'n'}|}{|g''_{m'n'}| + \text{median}\left(\left| g''_{p'q'} \right| \; | p'q' \epsilon \text{ subimage} \right)} < 1. \tag{7}$$

The directional values are sorted in 72 intervals. For each interval, the sum of the normalized complex values from (4) multiplied by their two quality measures from (6) and (7) is computed.

This histogram is smoothed with $B_{8x}^2 B_{4x}^2 B_{2x}^2 B_x^2$ and interpolated. The magnitude maximum on the interpolated histogram then gives the main squared gradient; the square root gives the main gradient; and the orthogonal to the main gradient defines the searched 180° ambiguous main direction.

Fig. 2 shows a sample histogram from a 10-km subimage from Fig. 1. All intervals are populated, but there is a distinct maximum defining the main squared gradient.

It should be noted that if multiple relative maxima are present in the histogram, all of them could be used to retrieve a direction. It should be noted as well that the derived directions are not quantized.

E. Accuracy of the Main Directions

The accuracy of the local gradients method was tested with artificial SAR images. Test patterns were created on an array with 400×400 points simulating a 5×5 km^2 subimage of an ERS SAR PRI. The test patterns show sine waves with a constant wavelength of 1 km or with varying wavelengths of 1 km at the center. Fig. 3 shows both types of test images smoothed and reduced to 100-m pixel size. The test images were processed as described in this section, and the magnitude of the directional errors were less than 0.25°, except for the pattern with a constant wavelength of 1 km where 400-m pixels were used. Clearly, a pattern with 1-km wavelength is not adequately sampled with

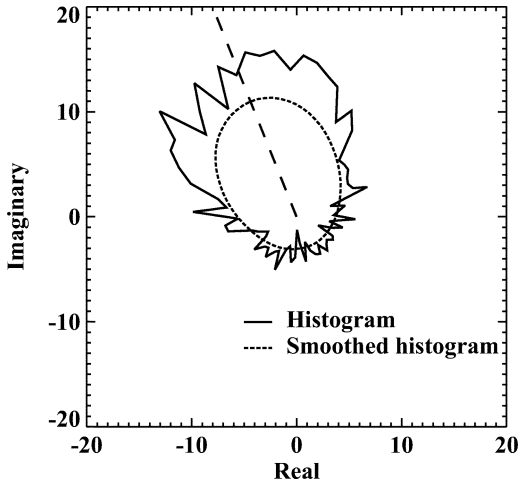

Fig. 2. Histogram of weighted and squared local gradients. The wind direction is determined from the magnitude maximum of the smoothed histogram.

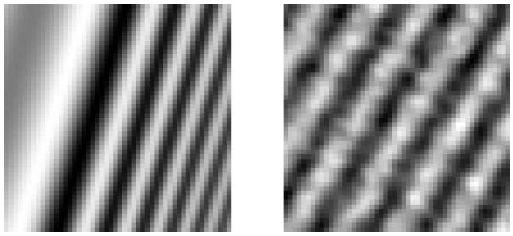

(a) (b)

Fig. 3. Smoothed 5×5 km^2 artificial test images reduced to 100-m pixel size. The left image shows a variable wavelength test pattern, while the right shows a pattern with constant wavelength and noise.

400-m pixels. Next the SAR typical speckle noise was applied to the test images, increasing the magnitude of the errors to about 1° with the same exception. The directional errors start to increase when the ratio of the amplitude of the test wave pattern to its average becomes less than 1/50. So, the anticipated accuracy of the method, close to 1°, is quite high.

F. High-Resolution Examples

Fig. 4 shows a 10×10 km^2 subimage close to the center of Fig. 1. Wind directions are computed from 100-m pixels on a 1-km grid. As computing local gradients involves further smoothing and reduction, at most 25 values are available for the histograms. Due to the low number of gradients available, secondary maxima in the histogram occur more frequently. Again, directional ambiguities were removed by manually selecting unique directions in some of the subimages and aligning the rest automatically. Dark and white arrows indicate discarded and accepted wind vectors, resepctively. The arrows are scaled with the wind speed, which is approximately 5 m/s in the average. It is obvious that the computed directions are not random. The general direction is diagonal, as was to be expected referring to Fig. 1. It seems the white arrows form a wind field that follows the course of the channel. Figs. 5 and 6 show an ERS-2 image from February 13, 2000, 10 : 50 of the Sogne Fjord in Norway, image center at 61.1° N and 5.3° E. The area is on the western side of an atmospheric low. Wind shadows visible in the image indicate the wind direction being from left to right. Computed from 100-m pixels, the white arrows form

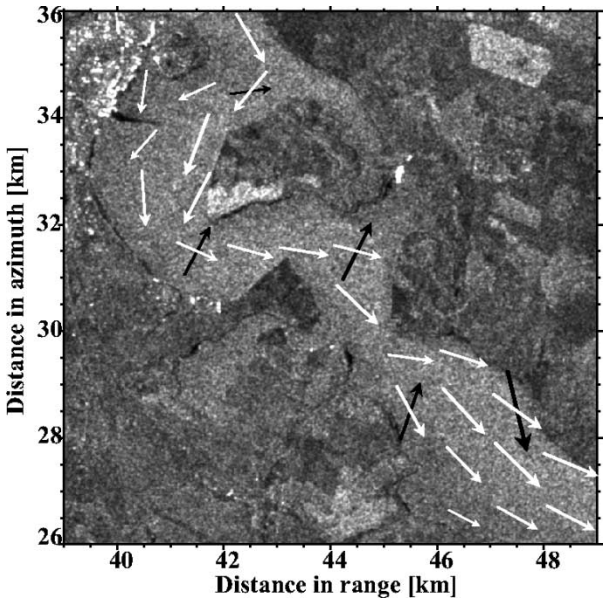

Fig. 4. Wind field in Der Bodden that separates Rügen from the mainland. Black arrows indicate rejected wind vectors, and the white arrows form a wind field that follows the channel. Mean wind speed is about 5 m/s.

wind fields on 20-, 10-, 5-, 2-, and 1-km grids that are strongly influenced by orography. The number of gradients available for the histograms varies from several thousand to less than 25 per subimage. Unique directions are obtained similar as before by selecting directions for one or two subimages and aligning the rest. Again, dark and white arrows indicate discarded and accepted wind vectors, resepctively. The arrows are scaled with the wind speed, which is around 6 m/s. Directions retrieved from a spectral method are indicated by black bars. Both directions agree to some extent. Agreement is best on large subimages, but even for 1-km subimages, there are a few areas with good concent.

III. Image Filtering

Fig. 7 shows an ERS-1 SAR image of a storm in the German Bight. There are dry wadden areas and linear features caused by tidal currents that need to be located. This can be done automatically using results and intermediate results from the computation of the local gradients. In Section III-A, four parameters are defined that do not depend on the particular image product, incidence angle, wind speed, and so on. By comparing the histograms of these parameters from images with nonwind generated features and the histograms from images without them, the parameter ranges indicating bad values, good values, and the transitions were identified. The four parameters are then combined to a quality measure (22) that assumes values from zero to one. Gradients are considered unusable where a revision of this measure is less than a threshold of 0.6 for an area of at least 1 km^2, or where a small object, e.g., a ship, is in the image. The algorithm used for revising the measure is detailed in Section III-B. Fig. 8 shows the result of the image filtering for the SAR image shown in Fig. 7. Areas in black and light gray are considered unusable by the image filter. Areas in white and light gray are land, according to a coastline database. The dry wadden areas and linear features caused by tidal currents

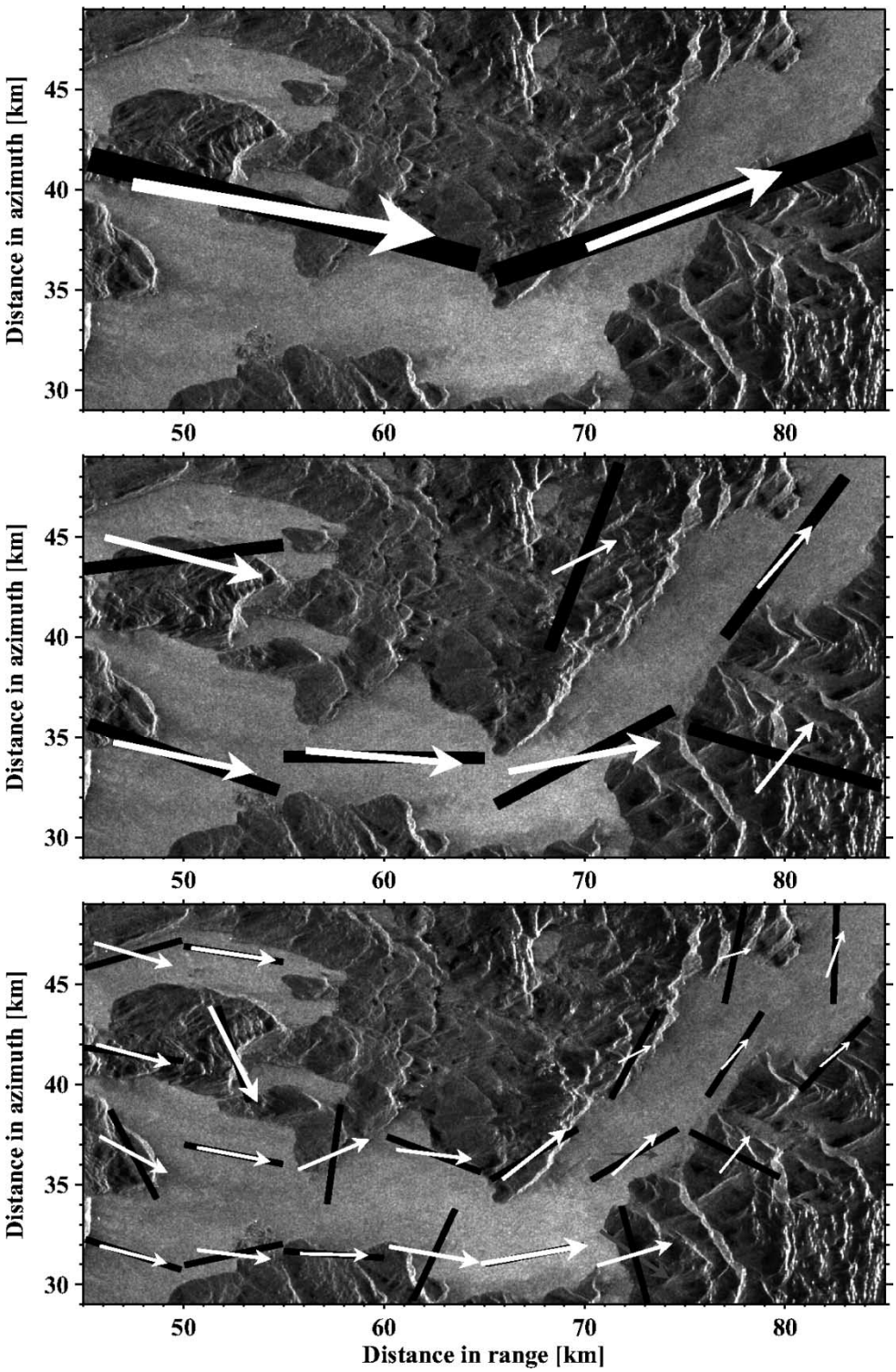

Fig. 5. ERS-2 SAR image of the Sogne Fjord from February 13, 2000, 10:50, image center at 61.1° N and 5.3°, with wind fields computed on 20×20 km^2, 10×10 km^2, and 5×5 km^2 subimages, indicated by white arrows. Wind directions were computed with local gradients from 100-m pixels. Black bars give wind direction computed with a spectral method.

are successfully located. However, land is not always detected. Thus, this image filtering would not spare the use of a coastline dataset.

A. Quality Parameters

The first parameter defined (12) is the quotient of the standard deviation (11) and the mean (9) of some neighborhood of every point of the smoothed and reduced image A' (8). The local second moment of the amplitude image A' is computed according to (10). Extended areas that are not open ocean surfaces, as land, tidal flats, or sea ice are detected in this way (13), but edges or very narrow features are not

$$A' = (a'_{m'n'}) = R_{|2}(A) \tag{8}$$

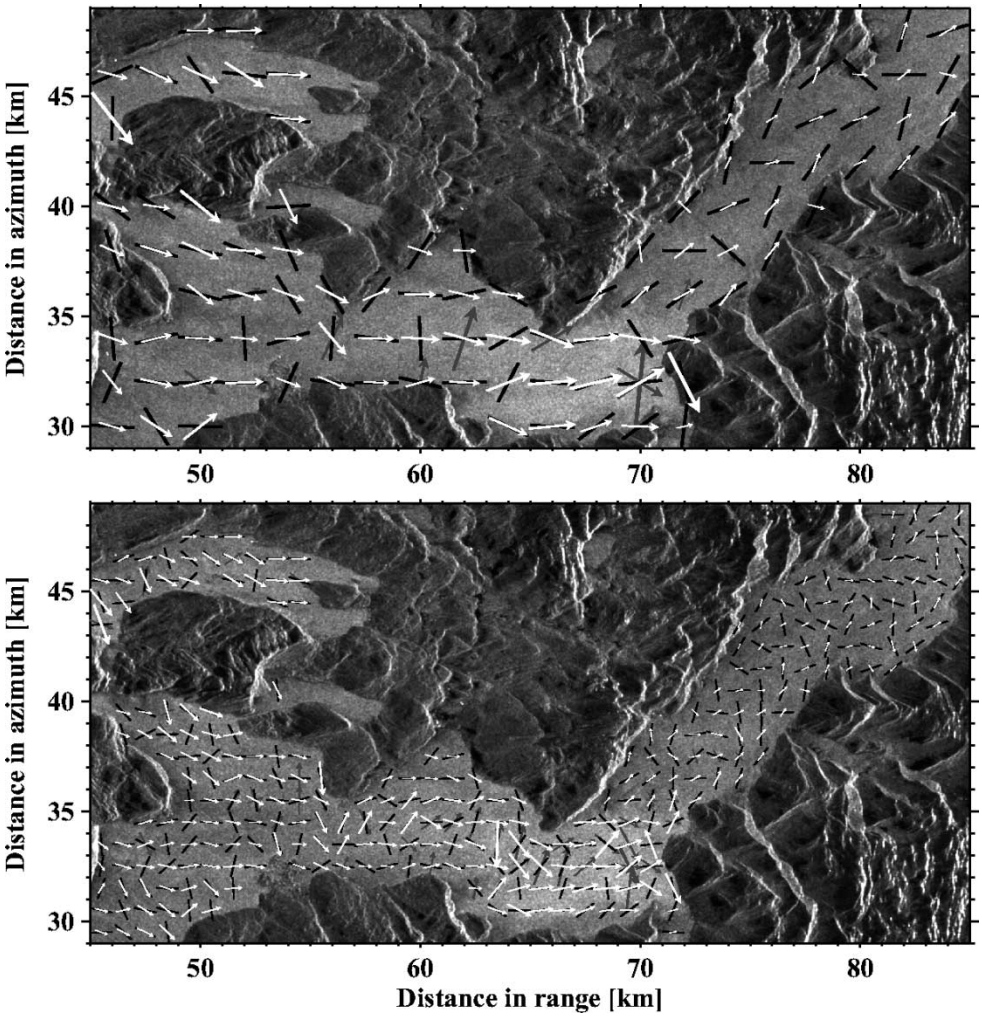

Fig. 6. ERS-2 SAR image of the Sogne Fjord from February 13, 2000, 10 : 50, image center at 61.1° N and 5.3°, with wind fields computed from 2×2 km^2, and 1×1 km^2 subimages, indicated by white arrows. Wind directions were computed with local gradients from 100-m pixels. Black bars give wind direction computed with a spectral method.

$$J = (j_{m'n'}) = M(A') \tag{9}$$

$$J' = (j'_{m'n'}) = M\left(\left(a'^{2}_{m'n'}\right)\right) \tag{10}$$

$$J'' = (j''_{m'n'}) = \left(\sqrt{j'_{m'n'} - j^2_{m'n'}}\right) \tag{11}$$

$$P_1 = \left(p_{1_{m'n'}}\right) = \left(\frac{j''_{m'n'}}{j_{m'n'}}\right) \tag{12}$$

$$f_{1_{m'n'}} = \begin{cases} 0, & p_{1_{m'n'}} > 0.055 \\ 1, & p_{1_{m'n'}} < 0.035 \\ \text{linear}, & \text{else.} \end{cases} \tag{13}$$

The second parameter (15) is the squared quotient of the high-pass filtered image (14) and the local mean (9). This corresponds to the Laplace pyramid introduced in chapter 5 of [12]. The measure (16) detects the interior of narrow image features, as slicks, internal waves, or fronts.

$$K = (k_{m'n'}) = (I - E_{|2}R_{|2})(A') \tag{14}$$

$$P_2 = \left(p_{2_{m'n'}}\right) = \left(\frac{k^2_{m'n'}}{j^2_{m'n'}}\right) \tag{15}$$

$$f_{2_{m'n'}} = \begin{cases} 0, & p_{2_{m'n'}} > 0.0006 \\ 1, & p_{2_{m'n'}} < 0.0004 \\ \text{linear} & \text{else.} \end{cases} \tag{16}$$

The third parameter (18) is the quotient of the magnitude of the squared local gradient (5) and its local mean (17). This measure (19) detects edges of narrow image features, and point targets give a particular strong signal.

$$G'''' = (g''''_{m'n'}) = M(G''') \tag{17}$$

$$P_3 = \left(p_{3_{m'n'}}\right) = \left(\frac{g'''_{m'n'}}{g''''_{m'n'}}\right) \tag{18}$$

$$f_{3_{m'n'}} = \begin{cases} 0, & p_{3_{m'n'}} > 1.6 \\ 1, & p_{3_{m'n'}} < 1.2 \\ \text{linear} & \text{else.} \end{cases} \tag{19}$$

The last parameter is the square root of the coherency (6). It is largest on well defined edges. The measure (21) detects the edges of narrow image features, as slicks, internal waves, or fronts.

$$P_4 = \left(p_{4_{m'n'}}\right) = (\sqrt{c_{m'n'}}) \tag{20}$$

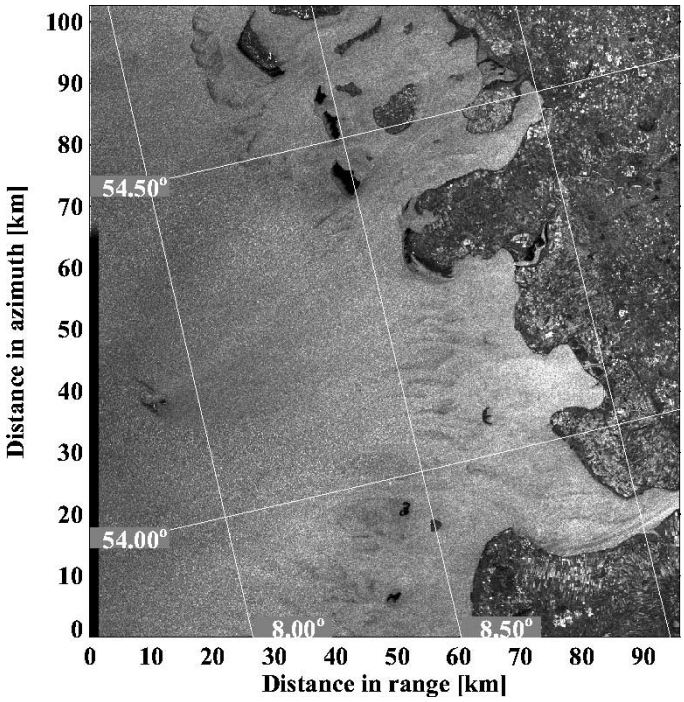

Fig. 7. ERS-1 SAR image of a storm in the German Bight from January 27, 1994 10 : 25. Dry tidelands and structures caused by tidal currents need to be located.

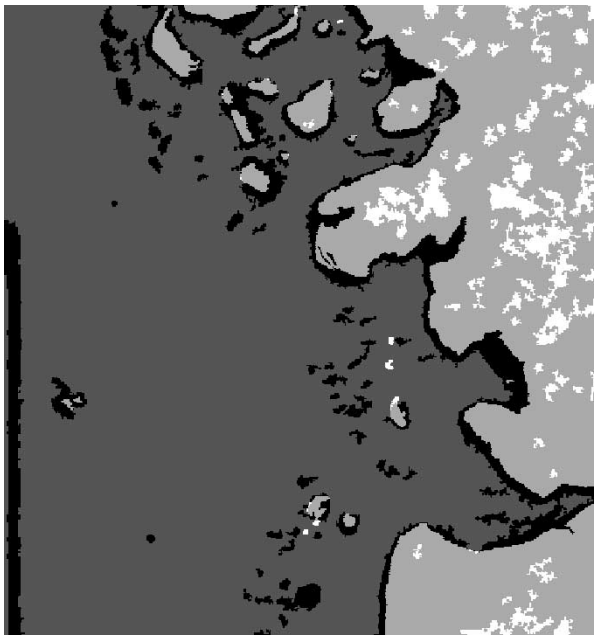

Fig. 8. Mask generated from the quality measures. White and light gray cover land as extracted from a coastline database. Light gray and black cover areas not considered for directional analysis, because they are flagged in the image filtering. Dark gray are the usable areas.

$$f_{4_{m'n'}} = \begin{cases} 0, & p_{4_{m'n'}} > 0.63 \\ 1, & p_{4_{m'n'}} < 0.53 \\ \text{linear} & \text{else.} \end{cases} \tag{21}$$

The four measures (13), (16), (19), (21) are combined by computing the root-mean-square average (22)

$$F = (f_{m'n'}) = \left(\sqrt{\frac{1}{4} \sum_{i=1}^{4} f_{i_{m'n'}}^2} \right). \tag{22}$$

B. Revision of the Filter

Comparing the combined measure (22) to a threshold of 0.6 gives a somewhat ragged distribution of bad points. There will be plenty of small clusters with no corresponding features in the amplitude image, and some lines of small clusters that correspond for instance with fronts. After connecting the cluster lines the remaining isolated clusters could be removed by requiring a minimal size for them. Those clusters corresponding to small objects such as ships or oil rigs have to be identified separately.

The linking of clusters can be achieved by referring to the adjacent pixels in the image with doubled pixel size, because the clusters tend to combine to lines there. Hence, the algorithm below proceeding from large pixel sizes to small ones will link the cluster lines.

1) The measures are computed for pixel sizes of $1600 \times 1600\ \mathrm{m}^2$, $800 \times 800\ \mathrm{m}^2$, $400 \times 400\ \mathrm{m}^2$, and $200 \times 200\ \mathrm{m}^2$.
2) For pixel sizes of $800 \times 800\ \mathrm{m}^2$, $400 \times 400\ \mathrm{m}^2$, and $200 \times 200\ \mathrm{m}^2$, where the measure of a reduced image is available, it is merged with the measure just computed in step 1). This means the measure of any pixel is averaged with the measure of that one of the four adjacent coarser pixels that is closest to its own original value.
3) Points with a measure of at least 0.6 are considered usable.
4) Connected usable points, that represent an area of less than $1\ \mathrm{km}^2$, are changed to unusable. This applies for pixel sizes of $800 \times 800\ \mathrm{m}^2$, $400 \times 400\ \mathrm{m}^2$, and $200 \times 200\ \mathrm{m}^2$, where the number of required pixels is 2, 7, and 25. Pixels are considered to be connected when they have a common side.
5) Connected unusable points, that represent an area less than $1\ \mathrm{km}^2$, are changed to usable.
6) For pixel sizes of $1600 \times 1600\ \mathrm{m}^2$, $800 \times 800\ \mathrm{m}^2$, and $400 \times 400\ \mathrm{m}^2$ the measures of connected unusable points, are replaced by their average. This information is used for the linking of the next smaller pixel size in step 2). Fig. 9 shows this stage on $200 \times 200\ \mathrm{m}^2$ pixels for the image shown in Fig. 7.
7) Small objects, as for example ships or oil rigs, have to be identified with the parameter in (18), because the corresponding clusters of bad points could have been removed in step 5). Hence, points with $p_3 > 5$, and their neighborhood are flagged unusable. This completes the information required in Section II-C.

IV. Interpretation

The local gradients method comes up with at least three 180° ambiguous suggestions for the wind directions stemming from the different pixel sizes used for the analysis. From Section II-D

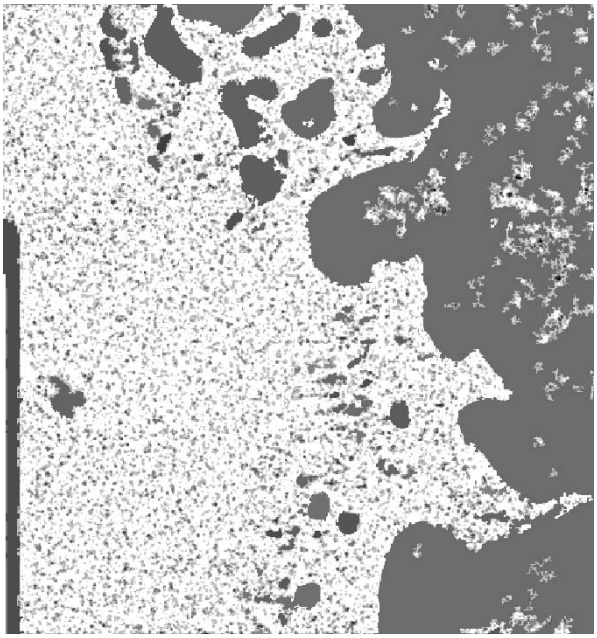

Fig. 9. Image quality, the brighter the points the better the quality. Connected unusable points have the same color.

it is known that the directions of patterns that are present in the image are accurately measured, but from a noisy image without any structure, a direction will be suggested as well. Consequently, for a single area of interest it is not known whether the suggested direction is related to wind, but looking at the context it becomes clear that the derived directions are nonrandom. Having a field of directions that form a flow pattern therefore strongly indicates physical reasons. When the produced field additionally is aligned with obvious wind features as shadows or visible rolls the confidence grows. Considering the wind speed computed with the suggested directions helps the interpretation, as for example in Figs. 4 and 6 some of the discarded wind vectors show unfitting large wind speeds.

The available experience suggests to take 100-m pixels for shallow seas, that are sheltered against long swell, as are the North and the Baltic Sea. Images of open seas which show the signature of long ocean waves, e.g., the Norwegian Sea are best smoothed and sampled to 200-m pixels. Pixel sizes of 400 m were only used in some rare cases.

V. Summary

A new method is at hand for estimating the wind directions directly from SAR images. It gains robustness, flexibility, and spatial resolution by direct evaluation of the amplitude image. Together with external topographic information, the proposed image filter localizes the areas in SAR images that show nonwind features and excludes them from evaluation. This enables SAR wind evaluation directly at the coastline and over narrow inland waters. The investigated subimages may be tailored to match the grid cells of numerical meteorological models, thus allowing comparison with or assimilation into models without spatial interpolation. The error in estimating directions of patterns in artificial SAR images is about 1° using an appropriate pixel size. The accuracy in real SAR images should be so well that the difference between the pattern direction and the wind direction dominates the overall directional error. Hence, the proposed method gives a promising alternative to the established techniques of wind direction estimation. The new method is designed to work with subimages of arbitrary size down to 1 km^2 without modifications. No manual intervention is required until the method presents directions based on 100-, 200-, and 400-m pixels, usually one per pixel size and subimage. Removal of the 180° ambiguity is done semiautomatically by manually selecting unique directions on some subimages and automatically choosing the best aligned directions in the remaining subimages.

Appendix

The descriptions of the algorithms are based on several basic operations that are given below. Sums and differences of operations are to be interpreted as pointwise sums or differences of the images resulting from the operations. Products with scalars are to read as the pointwise product of the scalar and the image resulting from the operation. Products of operators are to be read as applying the operations one after the other, rightmost first. Powers of operators denote multiple application of that operator. The identity is denoted as I. Most of the employed operators are convolution kernels. Let H be an operator and A an image. Then, $A' = HA$ is defined pointwise by

$$a'_{mn} = \sum_{k=-r}^{r} \sum_{l=-s}^{s} h_{-k,-l} a_{m+k,n+l}. \tag{23}$$

From the definition, it is clear that the points at the image boundaries cannot be defined accurately. The undefined values are either substituted by zeroes or by copying the closest defined value. For smoothing operations in various directions, binomial operators are used to replace the generic operator H in (23)

$$B_x = \frac{1}{2}(1 \quad 1) \tag{24}$$

$$B_x^2 = \frac{1}{4}(1 \quad 2 \quad 1) \tag{25}$$

$$B_y^2 = \frac{1}{4}\begin{pmatrix} 1 \\ 2 \\ 1 \end{pmatrix} \tag{26}$$

$$B_{x+y}^2 = \frac{1}{4}\begin{pmatrix} 0 & 0 & 1 \\ 0 & 2 & 0 \\ 1 & 0 & 0 \end{pmatrix} \tag{27}$$

$$B_{x-y}^2 = \frac{1}{4}\begin{pmatrix} 1 & 0 & 0 \\ 0 & 2 & 0 \\ 0 & 0 & 1 \end{pmatrix} \tag{28}$$

$$B^2 = \frac{1}{16}\begin{pmatrix} 1 & 2 & 1 \\ 2 & 4 & 2 \\ 1 & 2 & 1 \end{pmatrix} = B_y^2 B_x^2. \tag{29}$$

A numerical subscript n means that the dimensions of the convolution kernel are extended by adding $n-1$ zero rows and columns, e.g.,

$$B_2^2 = \frac{1}{16}\begin{pmatrix} 1 & 0 & 2 & 0 & 1 \\ 0 & 0 & 0 & 0 & 0 \\ 2 & 0 & 4 & 0 & 2 \\ 0 & 0 & 0 & 0 & 0 \\ 1 & 0 & 2 & 0 & 1 \end{pmatrix} \tag{30}$$

$$B_{4x}^2 = \frac{1}{4}(1 \quad 0 \quad 0 \quad 0 \quad 2 \quad 0 \quad 0 \quad 0 \quad 1). \tag{31}$$

A local mean is computed with the following operator:

$$M = B_2^4 B^4. \tag{32}$$

Reduction of an image is denoted by $S_{|d}$. The subscript with the vertical line gives the factor of the image reduction, e.g., $S_{|2}$ means an image reduction to half dimensions. Most frequently, image reduction is used together with smoothing

$$R_{|2} = B^2 S_{|2} B^4. \tag{33}$$

Expanding of an image by a factor of two is done by first copying and interpolating intermediate columns of the image as follows:

$$\begin{aligned} \mathfrak{a}'_{m'} &= \mathfrak{a}_m \\ \mathfrak{a}'_{m'+1} &= \frac{1}{16}(-\mathfrak{a}_{m-1} + 9\mathfrak{a}_m + 9\mathfrak{a}_{m+1} - \mathfrak{a}_{m+2}) \\ \mathfrak{a}'_{m'+2} &= \mathfrak{a}_{m+1}. \end{aligned} \tag{34}$$

The same is done with the rows of the resulting image. The composed operation is denoted as $E_{|2}$.

ACKNOWLEDGMENT

This work was enabled by the European Space Agency, who supplied ERS-1 and ERS-2 SAR data under the projects AO2.D113 and AOE.220.

REFERENCES

[1] J. Horstmann, S. Lehner, W. Koch, and R. Tonboe, "Computation of wind vectors over the ocean using spaceborne synthetic aperture radar," *Johns Hopkins APL Tech. Dig.*, vol. 21, no. 1, pp. 100–107, 2000.

[2] D. R. Thompson and R. C. Beal, "Mapping of mesoscale and submesocale wind fields using synthetic aperture radar," *Johns Hopkins APL Tech. Dig.*, vol. 21, no. 1, pp. 58–67, 2000.

[3] F. Monaldo, "The Alaska SAR demonstration and near-real-time synthetic aperture radar winds," *John Hopkins APL Tech. Dig.*, vol. 21, no. 1, pp. 75–79, 2000.

[4] T. G. Gerling, "Structure of the surface wind field from Seasat SAR," *J. Geophys. Res.*, vol. 91, pp. 2308–2320, 1986.

[5] W. Alpers and B. Brümmer, "Atmospheric boundary layer rolls observed by the synthetic aperture radar aboard the ERS-1 satellite," *J. Geophys. Res.*, vol. 99, pp. 12 613–12 621, 1994.

[6] G. Levy and R. A. Brown, "Detecting planetary boundary layer rolls from SAR," in *Remote Sensing of the Pacific Ocean From Satellites*, R. A. Brown, Ed., 1998, pp. 128–134.

[7] C. C. Wackerman, C. L. Rufenach, R. Schuchman, J. A. Johannessen, and K. Davidson, "Wind vector retrieval using ERS-1 synthetic aperture radar imagery," *J. Geophys. Res.*, vol. 34, pp. 1343–1352, 1996.

[8] P. W. Vachon and F. W. Dobson, "Validation of wind vector retrieval from ERS-1 SAR images over the ocean," *Global Atmos. Ocean Syst.*, vol. 5, pp. 177–187, 1996.

[9] F. Fetterer, D. Gineris, and C. C. Wackerman, "Validating a scatterometer wind algorithm for ERS-1 SAR," *IEEE Trans. Geosci. Remote Sensing*, vol. 36, pp. 479–492, Mar. 1998.

[10] S. Lehner, J. Horstmann, W. Koch, and W. Rosenthal, "Mesoscale wind measurements using recalibrated ERS SAR images," *J. Geophys. Res.*, vol. 103, pp. 7847–7856, 1998.

[11] P. Wessel and W. H. F. Smith, "New version of the generic mapping tools released," *EOS Trans. Amer. Geophys. Union*, vol. 76, p. 329, 1995.

[12] B. Jähne, *Digital Image Processing. Concepts, Algorithms, and Scientific Applications*, 4th ed. Berlin, Germany: Springer-Verlag, 1997.

[13] W. Koch, "Semiautomatic assignment of high resolution wind directions in sar images," in *Proc. OCEANS Conf.*, vol. 3, Providence, RI, 2000, pp. 1775–1782.

Wolfgang Koch received the state examination in mathematics, physics, and educational science from the University of Hamburg, Hamburg, Germany, in 1988.

In 1987, he joined the boundary layer group at GKSS Research Center, Geesthacht, Germany. He has participated in numerous wave modeling projects, worked in verification of wind and wave measurements with altimeters, and is currently in the Institute for Coastal Research working on wind estimation from SAR images.